Journal of
Polymer Materials

Tech Science Press

https://doi.org/10.32604/jpm.2026.077100

ARTICLE

Synergistic Emulsifier System Based on Molecular Design for Ultra-Low Oil-to-Water Ratio Oil-Based Drilling Fluids

Junping Wang[1,2], **Mingbiao Xu**[3,*] **and Wei Xiao**[1,*]

[1]College of Chemistry & Environmental Engineering, Yangtze University, Jingzhou, China
[2]Western Drilling Engineering Company of China National Petroleum Corporation, Urumqi, China
[3]School of Petroleum Engineering, Yangtze University, Wuhan, China

*Corresponding Authors: Mingbiao Xu. Email: xmb62@163.com; Wei Xiao. Email: xwylyq2006@126.com

Received: 02 December 2025; Accepted: 06 February 2026; Published: 03 April 2026

ABSTRACT: Formulating oil-based drilling fluids (OBDFs) with an ultra-low oil-to-water ratio (OWR ≤ 60:40) presents a formidable stability challenge due to the maximized interfacial area and intensified stress on the interfacial film under high-temperature, high-density conditions. To address this, we engineered a synergistic stabilization system through molecular and colloidal design. A novel hyperbranched polyamide emulsifier (epoxidized soybean oil polyamide) (ESOP), synthesized from epoxidized soybean oil, exhibits superior thermal stability and interfacial activity due to its hyperbranched architecture. Combined with calcium petroleum sulfonate (CPS) and hydrophobic nanosilica (HNs), it enables a high-performance OBDF with an ultra-low OWR of 60:40. The results show that the optimized formula achieves an excellent demulsification voltage of 1290 V, an ultra-low HTHP fluid loss of 1.5 mL, a yield point of 12.9 Pa, and a superior sag factor (SF) of 0.504, outperforming both base and commercial systems. Mechanistic studies reveal a multiscale stabilization strategy involving a dense composite interfacial film, Pickering stabilization, a 3D network, and a unique thermally triggered self-reinforcement effect. This work not only provides a cost-effective OBDF formulation but, more importantly, establishes a molecular topology engineering paradigm for stabilizing complex industrial fluids under extreme conditions.

KEYWORDS: Oil-based drilling fluid; low oil-to-water ratio; emulsifier; synergistic effect; molecular topology design

1 Introduction

Drilling fluid performance is crucial for addressing challenges in the oil and gas industry. Typically, drilling fluids can be categorized into water-based drilling fluids (WBDFs), OBDFs, and synthetic-based drilling fluids (SBDFs). While WBDFs are widely used due to their cost-effectiveness and environmental advantages, OBDFs are indispensable for more demanding applications [1–4]. OBDFs provide excellent lubrication, inhibition, thermal stability, and resistance to high temperatures, salts, and calcium contamination. These properties prevent shale hydration and well wall collapse, making OBDFs essential for unconventional, deep, and long horizontal wells [5–7]. Despite these advantages, the high cost of base oil and emulsifiers, difficulties in mudcake removal, and stringent environmental regulations have impeded their broader application [8–11]. A key strategy to reduce cost and environmental impact is to minimize the OWR. Conventional OBDFs typically contain 10%–20% water, whereas low-OWR formulations increase the water phase to 30%–40% [5]. Reducing the OWR is crucial for cost-effective, environmentally sustainable OBDFs, driving demand for ultra-low OWR formulations. However, this reduction can impair rheological

properties and emulsion stability, especially at prolonged high temperatures, leading to emulsifier failure, barite sedimentation, and drilling fluid failure [12–15].

Researchers have developed various emulsifiers, including commercial polymers and pH-sensitive reversible emulsifiers, to enhance OBDF performance [16–20]. Pu et al. [21] improved the emulsion's stability by introducing hydrophilic nanosilica. The results showed that nano-silica could effectively improve the flow pattern of the drilling fluid. Compared to the system without nano-silica, nano-silica increased the demulsification voltage of the drilling fluid system to 874 V under aging conditions at 140°C and reduced the filtrate loss rate by up to 81.8%. However, conventional and most commercial emulsifiers often fail under such demanding conditions due to inherent molecular limitations: their linear or weakly branched structures are prone to thermal degradation and desorption at elevated temperatures, leading to the collapse of the interfacial film. These limitations are particularly acute in ultra-low OWR, high-density systems, stemming from both inherent structural flaws and derived performance deficits. Conventional architectures lack thermal and mechanical stability at the interface, while even advanced formulations struggle with long-term decay, rheological trade-offs, contamination sensitivity, and environmental impact. Therefore, the development of emulsifiers with three-dimensional topological structures has emerged as a promising strategy to address this challenge. Star-shaped polymers exhibit a relatively regular structure, yet the density of functional sites remains comparatively low. Well-established research confirms that achieving perfect dendrimers requires a synthetically challenging and laborious process. Consequently, their high manufacturing cost prohibits widespread availability, posing the primary impediment to their broader application [22]. In contrast, hyperbranched polymers are a kind of polymer with a three-dimensional structure—offering a more economical synthesis route while retaining many desirable properties of dendrimers, such as low melt viscosity, high solubility, and a large number of terminal functional groups [23]. A key limitation persists for ultra-low OWR OBDFs under extreme conditions: even with advanced high-temperature emulsifiers like aromatic/sulfonated modifiers and nanoparticle stabilizers, the interfacial film often lacks sufficient strength and packing density [24–26]. The fundamental challenge in such systems stems from the drastically increased oil-water interfacial area when the oil phase is minimized. This expansive interface places extraordinary demands on the emulsifier's ability to form a dense, cohesive, and mechanically robust film that can withstand elevated temperatures and shear. Hyperbranched polymers (HBPs) represent a promising candidate in this regard, and initial studies, such as the work by Wei [27], have confirmed the feasibility of hyperbranched polyamides for OBDFs, reporting demulsification voltages above 800 V at 180°C. However, a critical gap persists between this promising topology and the specific demands of ultra-low OWR systems. Existing studies on HBPs for drilling fluids have predominantly been validated under conditions that differ fundamentally from the scenario targeted here—often employing different base fluids (e.g., synthetic-based systems) or higher, more forgiving OWRs. Under these conditions, the interfacial stress is comparatively lower, and stabilization often emphasizes bulk-phase viscositying effects.

To address the paramount challenge of stabilizing ultra-low OWR (60:40) OBDFs under high-temperature, high-density conditions—where maximized interfacial area intensifies stress on the interfacial film—this study employs a combined strategy of molecular topology engineering and synergistic colloidal formulation. We developed a novel hyperbranched polyamide emulsifier (ESOP) from ESO, featuring rigid-flexible segments and stable amide bonds for enhanced thermal stability and multi-site interfacial anchoring. Moving beyond single-component solutions, ESOP was synergized with CPS and HNs to formulate a 60:40 OWR fluid that maintains exceptional stability after dynamic aging at 180°C. Comprehensive characterization reveals a multi-scale stabilization mechanism, including a composite interfacial film and a unique thermally-triggered self-reinforcement effect critical under extreme OWR conditions. This work establishes

a targeted design paradigm linking hyperbranched topology, synergistic formulation, and high performance for ultra-low OWR OBDFs under extreme downhole conditions.

2 Materials and Methods

2.1 Materials

The experimental reagents and instruments used in this work are listed in Tables 1 and 2.

Table 1: Experimental reagents.

Material	Purity/Grade	Supplier
Epoxidized soybean oil (ESO)	95.0%, M_w = 1000	Wuhan Hengjiu Chemical Co., Ltd.
Diethylenetriamine (DETA)	99.0%	Shandong Hongyang Chemical Co., Ltd.
Calcium petroleum sulfonate	99.0%	Hubei Baidu Chemical Co., Ltd.
p-Toluenesulfonic acid	98.0%	Aladdin, Shanghai, China
Calcium hydroxide	99.0%	Aladdin, Shanghai, China
Hydrophobic nanosilica	98.0%	Shouguang Changtai New Materials Co., Ltd.
Oxidized asphalt	99.0%	Shandong Tonglan Chemical Co., Ltd.
Organobentonite	99.0%	Shouguang Changtai New Materials Co., Ltd.
Barite	95.0%	Tianjin Yandong Haotian Mineral Products Co., Ltd.
Tetrahydrofuran (THF)	99.9%	Merck, Rahway, NJ, USA
Sulfonated polyacrylamide (S-PAM)	98.0%	Shandong Noah Biological Technology Co., Ltd.
Commercial high-temperature primary emulsifier (HRP-1)	/	CNOOC Energy Technology & Services Ltd.

Table 2: Experimental instruments.

Instrument	Model	Manufacturer
Fourier-transform infrared (FTIR) spectrometer	Nicolet iN10	Thermo Fisher Scientific, Shanghai
Thermogravimetric analyzer(TGA)	HQG-1SK	Beijing Hengji Experimental Equipment Co., Ltd., Beijing
Six-speed viscometer	ZNN-D6	Changzhou Dedu Precision Instrument Co., Ltd., Jiangsu
Gel permeation chromatography	Agilent 1260 Infinity	Agilent Technologies, Inc., Santa Clara, CA, USA
High-temperature roller heating furnace	XGRL-4A	Huangdao Senweida Electromechanical Equipment Business Department, Qingdao
Electrical stability tester	DWY-2	Qingdao Haitongda Special Instrument Co., Ltd., Qingdao
HTHP filtration tester	GGS71-B	Hengtaida Mechanical and Electrical Equipment Co., Ltd., Qingdao

(Continued)

Table 2 (continued)

Instrument	Model	Manufacturer
Nanoparticle size potentiometer	Litesizer 500	Anton Paar, Shanghai
Spinning Drop Tensiometer	YP-ZL10	Shandong Jiuzhang Scientific Instrument Co., Ltd.
Laser Diffraction Particle Size Analyzer	Mastersizer 3000	Malvern Panalytical
Adjustable-angle static sag test stand	Custom-built	N/A

2.2 Synthesis of ESOP

A series of ESOP emulsifiers was synthesized with different ESO-to-DETA molar ratios (1:1, 1:1.2, 1:1.5, 1:1.8, 1:2). In a typical process, ESO and DETA at the desired molar ratio were added to a 250 mL four-necked round-bottom flask fitted with a mechanical stirrer, thermometer, Dean-Stark trap, and reflux condenser. The reaction mixture was first heated to 110°C–120°C for 2 h to promote the ring-opening reaction. Then, the temperature was increased to 160°C–180°C for 5 h to encourage polyamidation and dehydration. The reaction progress was tracked by titrating for the amine value. After completion and cooling below 100°C, any unreacted DETA was removed under reduced pressure (−0.01 MPa) at 120°C for 1.5 h. The process produced a viscous, brown-red product (98.5% yield) without further purification, labeled as ESOP-x (where 'x' indicates the DETA molar equivalent). The specific mass loadings of ESO and DETA corresponding to the different molar ratios are provided in Table 3.

Table 3: Specific loadings of reactants for the synthesis of ESOP.

Molar Ratio	ESO (g)	DETA (g)	Product Label
1:1	20.00	2.06	ESOP-1
1:1.2	20.00	2.48	ESOP-1.2
1:1.5	20.00	3.10	ESOP-1.5
1:1.8	20.00	3.71	ESOP-1.8
1:2	20.00	4.13	ESOP-2

The formation mechanism of the hyperbranched poly(amido amine) proceeds through two sequential and synergistic reactions: initially, the primary amine groups of diethylenetriamine act as nucleophiles, attacking the epoxide rings in ESO, which triggers a ring-opening reaction and yields β-hydroxyamine intermediates—this step establishes the molecular backbone and introduces critical branching points. Subsequently, at elevated temperatures, the amine groups undergo a polyamidation reaction with the ester linkages in the soybean oil backbone, forming highly thermally stable amide bonds via dehydration, ultimately leading to the construction of a hyperbranched polymer with a three-dimensional topological network. The essence of this cooperative mechanism lies in leveraging the multifunctionality of the monomers: the ring-opening addition builds the structural framework, while the subsequent polyamidation imparts reinforcement and stability to the architecture. Both ESO and DETA are multifunctional monomers. The above two reactions will occur alternately and competitively, eventually forming a three-dimensional hyperbranched network structure. Fig. 1a–c illustrates the structure formula for ESO and the reaction process.

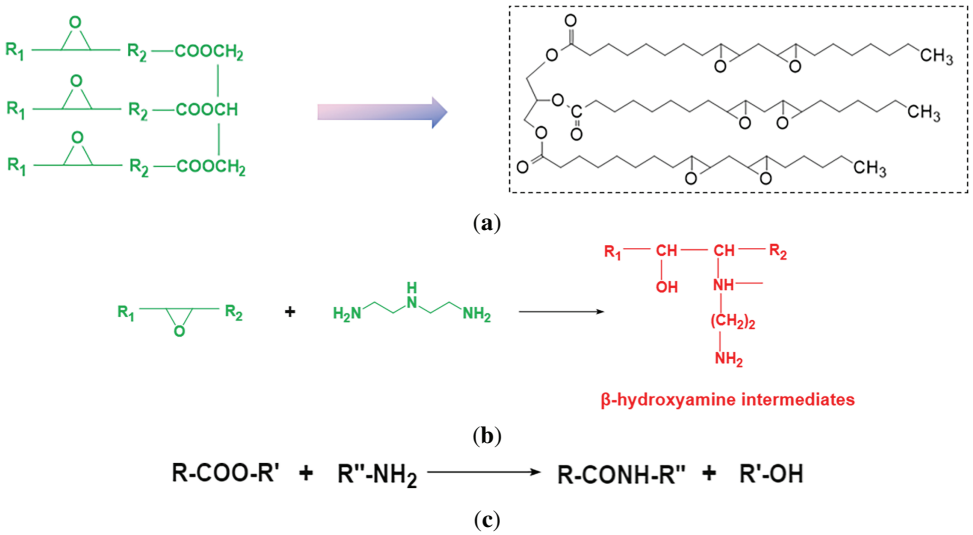

Figure 1: (**a**) Structure Formula of ESO (R_1 and R_2 represent the fatty acid chains). (**b**) Ring-opening addition reaction. (**c**) Polyamidation reaction.

2.3 Characterization

2.3.1 Fourier-Transform Infrared (FTIR) Spectroscopy

The molecular structure of the synthesized ESOP was analyzed using FTIR spectroscopy with a Nicolet iN10 spectrometer (Thermo Fisher Scientific) equipped with a diamond attenuated total reflectance (ATR) accessory. A small drop of the pure liquid ESOP sample was placed directly on the ATR crystal. Spectra were recorded over a wavenumber range of 4000 to 400 cm^{-1} with a resolution of 4 cm^{-1}, and 32 scans were averaged to achieve a high signal-to-noise ratio. The background spectrum was taken against clean air before measuring the sample.

2.3.2 Thermogravimetric Analysis (TGA)

Thermal stability was assessed using an HQG-1SK thermogravimetric analyzer. An Al_2O_3 crucible was zero-calibrated in the sample chamber. Precisely 20 mg of the sample was accurately weighed into an alumina crucible, which was then placed back in the chamber. The TGA program heated samples at 10°C/min under N_2 atmosphere to a final temperature of 650°C. Thermograms of ESOP were recorded and analyzed.

2.3.3 Molecular Weight Determination

GPC determined the molecular weight and molecular weight distribution of the synthesized ESOP. High-performance liquid chromatography (HPLC) grade THF was used as the eluent at a flow rate of 1.0 mL/min. The system was calibrated with narrow dispersity polystyrene standards. The sample was prepared by dissolving the product in THF at a concentration of approximately 2.0 mg/mL and then filtering it through a 0.45 μm PTFE syringe filter before injection.

2.4 Preparation and Formulation of OBDFs

The formulation design was guided by preliminary screening tests aimed at achieving a balance between emulsion stability, rheological properties, and filtration control at an ultra-low OWR of 60:40. The performance evaluation was conducted using oil-based drilling fluids with different OWRs. The base

formulation is summarized in Table 1. Three comparative systems were prepared: (1) a base fluid without CPS synergist, (2) a base fluid with a commercial emulsifier package replacing the ESOP/CPS system, and (3) the base fluid with the synthesized ESOP/CPS synergistic emulsifier package.

The drilling fluids were prepared according to the addition order specified in Table 4. This specific addition sequence was designed to ensure the sequential dissolution and hydration of additives and the stepwise formation of a stable emulsion structure, thereby preventing component incompatibility. Briefly, the base oil, emulsifier, and synergist were first mixed and stirred at 10,000 rpm for 20 min. Subsequently, the organoclay was added and mixed for an additional 30 min. Next, the wetting agent and lime were incorporated under stirring at 8000 rpm for 10 min. The $CaCl_2$ solution was then slowly introduced and emulsified at 10,000 rpm for 45 min to form a stable invert emulsion. Finally, the filtration loss additive was added and stirred at 8000 rpm for 20 min. After all additives were fully dispersed, barite was incrementally added at 4000–6000 rpm to weigh the system to the desired density (1.8 g/cm^3), and the mixture was homogenized at 10,000 rpm for 30 min to obtain the base slurry. For formulations containing HNs, 2 wt.% (by total fluid weight) HNs were added after the emulsification step and stirred for an additional 20 min to promote Pickering stabilization and nano-filling effects. For the comparative systems, the commercial emulsifier package was added at the recommended dosage and stirred before introducing the aqueous phase, while the synergist-free variant was prepared by omitting CPS and proportionally increasing the primary emulsifier. All samples were subjected to hot-rolling aging at specified temperatures (90°C, 120°C, 150°C, or 180°C) for 16 h to simulate downhole conditions. and after cooling and remixing, their performance was comprehensively evaluated in accordance with API 13B-2 standards.

Table 4: Base formulation for the oil-based drilling fluid.

Component	Function	Concentration	Addition Order
White Oil	Base Oil	To balance	1
30% $CaCl_2$ solution	Aqueous Phase	40%	4
ESOP Emulsifier	Primary Emulsifier	4.8 wt.% of oil phase	2
CPS	Synergist	3.2 wt.% of oil phase	2
Fatty alcohol phosphate ester	Wetting Agent	2.0 vol.% of total	5
Organoclay	Viscosifier	3.0 vol.% of total	3
lime (CaO)	Alkalinity Controller	3.5 vol.% of total	5
Filtration loss additive	Filtration Control	4.2 vol.% of total	6
Barite	Weighting Agent	To a density of 1.8 g/cm^3	7

Note: wt.% = weight percentage; vol.% = volume percentage.

2.5 Drilling Fluid Performance Evaluation

All performance evaluations detailed in this section were conducted in triplicate. The results are reported as the mean ± standard deviation to ensure statistical reliability.

2.5.1 Rheological Property Measurements

The drilling fluid samples were stirred at high speed (11,000 rpm) for 20–30 min in a slurry cup. Subsequently, the homogenized samples were transferred to the test cup of a ZNN-D6 six-speed rotational viscometer. Rheological parameters were measured sequentially at rotational speeds of 600, 300, 200, 100, 6, and 3 rev/min. Apparent viscosity (AV), plastic viscosity (PV), and yield point (YP) were calculated using the following standard formula [28], and repeated three times to get the average value.

$$AV = 0.5_{\Phi_{600}} \quad (1)$$

$$PV = \Phi_{600} \quad \Phi_{300} \quad (2)$$

$$YP = 0.511(\Phi_{300} - PV) \quad (3)$$

2.5.2 Electrical Stability Test (ES)

Emulsion stability was determined by measuring the dielectric demulsification voltage using a DWY-2 electrical stability tester according to the API recommended practice [13B-2]. The test was conducted as follows: A 50 mL homogeneous sample of the drilling fluid was placed into the test cup. The sample was then heated to and maintained at 55 ± 1°C in a constant-temperature water bath for at least 10 min, with gentle manual stirring immediately before testing to ensure uniformity. A concentric cylindrical electrode assembly was inserted into the sample. The voltage was increased linearly at a constant rate of 150 V/s until a sharp drop in current indicated emulsion breakdown, and the maximum voltage was recorded as the demulsification voltage [29]. This procedure was repeated three times on fresh samples, and the average value was reported.

2.5.3 HTHP FL Test

The HTHP FL method introduced in the literature is adopted for evaluation [30]. That is, different concentrations of ESOP were added to the OBDFs and stirred at 10,000 rpm for 20 min. The OBDFs were hot-rolled at 90°C, 120°C, 150°C, and 180°C for 16 h. After aging, the HTHP FL was determined using an HTHP filtration tester at the respective aging temperatures and under a pressure of 3.5 MPa.

2.5.4 Settlement Stability Test

The static sedimentation method introduced in the literature is usually adopted at the drilling site for evaluation, and the SF is used to quantify the sedimentation stability of the drilling fluid [31]. That is, test samples were subjected to hot rolling at predetermined temperatures for 16 h, followed by static aging at ambient conditions for 24 h. The densities of the top (ρ_{top}) and bottom (ρ_{bottom}) layers were then measured using a drilling fluid densimeter. The SF was calculated as follows [32]:

$$SF = \frac{\rho_{bottom}}{\rho_{bottom} + \rho_{top}} \quad (4)$$

An SF value greater than 0.52 indicates significant barite sedimentation within the drilling fluid system, while an SF value of 0.50 signifies optimal sag resistance with no noticeable settlement. To evaluate the effect of inclination angle, additional tests were conducted at vertical (0°), 45°, and horizontal (90°) orientations; the corresponding results are provided in Section 3.3.3.

2.5.5 Biological Toxicity Tests

The impact of OBDF on the environment was evaluated through biological toxicity tests, and the 50% effective concentration was determined using the fluorescent bacteria method [33]. The environmental impact of the OBDF was preliminarily evaluated through biological toxicity tests using the luminescent bacteria method, which is a standard and widely accepted assay in the drilling fluid industry for rapid screening. The 50% effective concentration (EC_{50}) was determined [34]. While multi-species ecotoxicity tests provide a more comprehensive assessment, the luminescent bacteria test offers a reliable and standardized indicator for initial environmental compatibility screening [35].

2.6 Interfacial and Microstructural Characterization

To elucidate the mechanisms underlying emulsion stabilization and sag resistance, complementary analyses of interfacial properties and colloidal microstructure were performed.

2.6.1 Interfacial Tension Measurement

The interfacial activity of the emulsifiers was quantified by measuring the equilibrium interfacial tension (IFT) between white oil and the 30 wt% $CaCl_2$ aqueous phase. Measurements were conducted using a spinning drop tensiometer at 25°C. IFT values were recorded for systems containing the individual components (ESOP, CPS) and their optimal synergistic mixture (ESOP:CPS = 60:40) to directly assess molecular synergy.

2.6.2 Emulsion Droplet Size Analysis

The microstructure of the freshly prepared invert emulsions was analyzed via laser diffraction using a particle size analyzer. To preserve the native droplet morphology and avoid disruption of the Pickering stabilization, samples were gently diluted with white oil and measured immediately without high-speed shearing or centrifugation. The volume-weighted mean diameter (D_{50}) and the polydispersity index (PDI) were reported to evaluate emulsion uniformity and stability.

2.6.3 Zeta Potential and Aggregate Size of Emulsifier Dispersions

The electrokinetic potential and size of emulsifier aggregates in the continuous oil phase were measured to investigate interfacial charge and thermally-induced changes. Samples were diluted 100-fold with white oil, ultrasonicated for 30 min to ensure dispersion, and centrifuged at 3000 rpm for 5 min to remove large particulates like barite and organoclay. The zeta potential and hydrodynamic diameter of the supernatant were then determined using Nanoparticle size potentiometer (Litesizer 500 Anton Paar, Shanghai) and Laser Diffraction Particle Size Analyzer (Mastersizer 3000, Malvern Panalytical).

3 Results and Discussion

3.1 Characterization

The molecular structure of the synthesized ESOP emulsifier and ESO was confirmed by FTIR spectroscopy, as shown in Fig. 2. The spectrum exhibited characteristic absorption bands corresponding to the expected functional groups of the hyperbranched polyamide. The broad peak at 3435 cm^{-1} is attributed to N-H stretching vibrations of secondary amide groups, indicating successful amidation. The distinct bands at 2952 and 2879 cm^{-1} correspond to asymmetric and symmetric C-H stretching vibrations of -CH_2- and -CH_3- groups, respectively, originating from the fatty acid chains of ESO and the alkyl segments of diethylenetriamine. A strong absorption observed at 1677 cm^{-1} is assigned to the C=O stretching vibration (amide I band), which is characteristic of the formed amide linkages [36]. The peak at 1459 cm^{-1} arises from C-H bending vibrations in methylene groups. Furthermore, the absorption at 1150 cm^{-1} is associated with C-O-C stretching vibrations of ether linkages, which may result from the residual or ring-opened structures of the epoxidized soybean oil [37]. Critically, the absence of characteristic epoxy ring absorption bands in the region of 820–910 cm^{-1} confirms the complete consumption of epoxy groups during the ring-opening and polyamidation reactions, verifying the successful synthesis of the target hyperbranched polyamide structure.

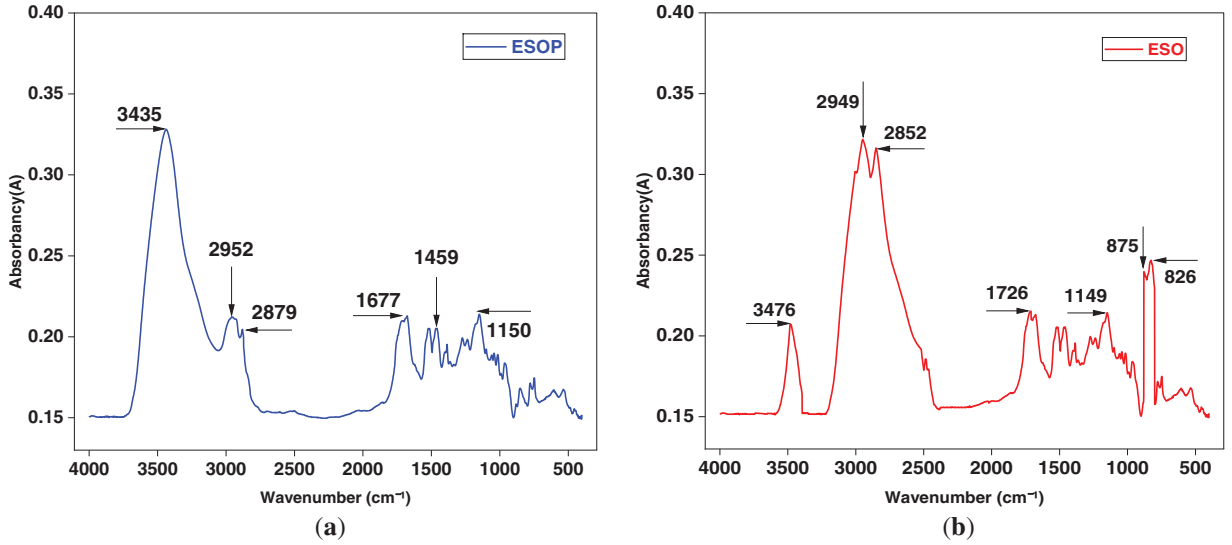

Figure 2: (**a**) FTIR spectrum of ESOP. (**b**) FTIR spectrum of ESO.

To rigorously evaluate the intrinsic thermal stability of the hyperbranched polyamide structure, ESOP was compared with sulfonated polyacrylamide (S-PAM). The TGA curves in Fig. 3 reveal that ESOP exhibits a multi-stage decomposition profile, demonstrating superior thermal resilience compared to S-PAM. The polymer showed excellent stability up to 200°C, with negligible mass loss (<3%), primarily due to the evaporation of moisture and volatile components [38]. A mass loss of 11.92% occurred between 200°C and 230°C, attributed to the decomposition of side groups and minor chains. Subsequently, a significant mass loss of 43.56% from 230°C to 490°C indicated the degradation of the primary polymer backbone, with decomposition occurring beyond 500°C. The derivative thermogravimetry (DTG) curves further clarify the decomposition stages. For ESOP, two distinct decomposition peaks are observed: the first peak at approximately 215°C corresponds to the decomposition of side groups and minor chains (mass loss of 11.92%), and the second peak at around 385°C is attributed to the degradation of the primary polymer backbone (mass loss of 43.56%). In contrast, S-PAM exhibits a sharp, single decomposition peak at about 185°C, indicating its rapid and extensive breakdown at a lower temperature. The distinct two-step decomposition profile of ESOP, in contrast to the single, sharp peak of S-PAM, provides direct thermal evidence of the structural heterogeneity within the hyperbranched architecture, where less stable peripheral groups decompose prior to the robust, cross-linked core. This robust thermal performance of ESOP can be attributed to its unique hyperbranched architecture rather than aromatic or sulfonic groups. The highly branched, three-dimensional molecular structure creates a multitude of strong hydrogen-bonding sites from the abundant amide groups. This extensive intermolecular hydrogen-bonding network significantly restricts the movement of molecular segments and increases the energy required for thermal decomposition. Furthermore, the compact, cross-linked nature of the hyperbranched topology inherently impedes the volatilization of decomposition fragments. Thus, the molecular topology itself is the primary factor conferring exceptional thermal stability to the ESOP polymer.

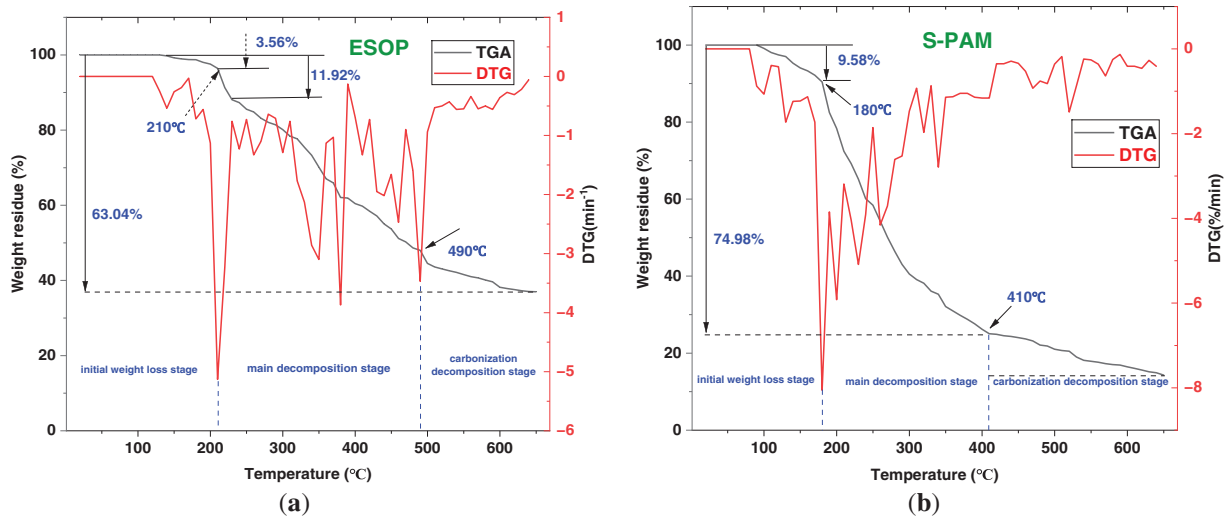

Figure 3: (**a**) TGA and DTG curves of the synthesized ESOP. (**b**) TGA and DTG curves of S-PAM.

3.2 Formulation Optimization

3.2.1 Optimization of ESOP Synthesis Ratio

GPC analysis (Table 5) the molar ratio of reactants significantly influences the molecular weight and its distribution of ESOP. When the ratio of ESO to DETA is 1:1, the amine is insufficient to fully open all epoxy groups and react with them, resulting in a highly branched structure and extensive cross-linking network. This leads to a very high M_w and an extremely wide PDI of up to 26.66, indicating that the product is a mixture of high molecular weight polymers and small molecular oligomers with non-uniform properties. When the ratio increases to 1:1.5, the excess DETA ensures the complete reaction of epoxy groups and effectively controls chain growth, primarily producing the desired low-molecular-weight polyamide amine. This results in moderate M_n and M_w with the narrowest PDI, indicating a well-defined structure and uniform composition. This feature is essential for forming a dense and stable interfacial film. When DETA is further in excess (1:1.8, 1:2), the excess amine acts as a 'chain terminator', greatly limiting the growth of molecular chains and leading to an excessively low molecular weight. Although the PDI remains narrow, these small molecules cannot form an interfacial film with sufficient mechanical strength. Therefore, ESOP-1.5 was identified as the optimal candidate for subsequent studies.

Table 5: The molecular weight of the ESOP series polymers.

Sample	M_n	M_w	M_z	PDI (M_w/M_n)
ESOP-1	1495	39,851	248,576	26.66
ESOP-1.2	2073	16,859	61,247	8.13
ESOP-1.5	4259	7768	12,521	1.82
ESOP-1.8	1786	2461	3684	1.38
ESOP-2	1152	1369	2143	1.19

3.2.2 Optimization of the Co-Emulsifier Ratio

To investigate the synergistic effect between ESOP and CPS, their molar ratio was optimized while keeping the total concentration at 8 wt% (relative to the oil phase). Five ratios of ESOP to CPS were tested:

100:0, 75:25, 60:40, 25:75, and 0:100. The drilling fluid formulations were otherwise identical to the base recipe described in Section 2.3. The optimal ratio of 60:40 was selected based on a comprehensive performance assessment, including electrical stability, SF, and HTHP FL, and was used in all subsequent comparative studies. The test results are shown in Table 6.

Table 6: Optimization of the ESOP-to-CPS molar ratio.

ESOP:CPS	Oil-to-Water Ratio	PV/(mPa·s)	YP/Pa	HTHP FL/mL	Demulsification Voltage/V	SF
100:0	80:20	24	4.2	7.6	762	0.527
75:25	80:20	29	7.1	3.9	995	0.519
60:40	80:20	33	8.9	2.5	1248	0.507
25:75	80:20	38	5.8	4.5	628	0.524
0:100	80:20	21	2.8	9.2	454	0.539

3.2.3 Optimization of Oil-to-Water Ratio

The optimization of the OWR, as summarized in Table 7, reveals a key trade-off between emulsion stability and rheological structure. As the water phase increases from 10% to 40%, the rheological properties (YP) are significantly improved due to the formation of a denser emulsion structure, which also enhances sag stability (SF approaching 0.506) and filtration control (HTHP FL as low as 1.7 mL). However, this comes with a gradual reduction in electrical stability, since the emulsifier system must stabilize a larger interfacial area. The formulation maintains excellent overall performance within the 70:30 to 60:40 range, where the demulsification voltage stays well above the 800 V threshold while achieving better sag resistance and filtration loss. The 50:50 ratio is identified as the operational limit, beyond which the interfacial film becomes overstretched, causing a sharp decline in electrical stability and a dangerous increase in the sag factor. Therefore, the OWR of 60:40 was established as the optimal value for this ultra-low-oil-phase system.

Table 7: Optimization of the OWR.

ESOP:CPS	Oil-to-Water Ratio	PV/mPa·s	YP/Pa	HTHP FL/mL	Demulsification Voltage/V	SF
60:40	90:10	27	4.1	4.3	1590	0.518
60:40	80:20	31	6.2	3.1	1421	0.515
60:40	70:30	39	8.9	1.9	1284	0.511
60:40	60:40	46	12.5	1.7	1258	0.506
60:40	50:50	59	16.9	2.6	694	0.529

3.3 Comprehensive Performance Evaluation of the Optimized OBDF System

In this section, the comprehensive performance of the developed OBDF system was evaluated and compared against base and commercial benchmarks. The assessment was conducted using three distinct formulations—a Base Formulation, a Commercial Emulsifier Formulation, and the ESOP-Optimized Formulation—all maintained at an ultra-low OWR of 60:40. These systems were subjected to hot-rolling at various temperatures (90°C, 120°C, 150°C, and 180°C) for 16 h to simulate severe downhole aging. The following subsections present a detailed analysis of the key performance metrics, including high-temperature tolerance, emulsification stability, sag resistance, and filtration control, measured after this aging process.

3.3.1 High-Temperature Tolerance and Overall Performance Comparison

The key performance metrics after the most severe aging at 180°C are summarized in Table 8. The ESOP-Optimized Formulation outperformed the other formulations across all key metrics (Table 8): it achieved a high YP of 9.8 Pa, indicating excellent cuttings transport capacity; a demulsification voltage of 1075 V, significantly higher than the industrial standard of 800 V; an ultra-low HTHP FL of 1.9 mL, reflecting superior filtration control; and an excellent SF of 0.509. These results confirm that the ESOP-optimized system effectively overcomes the performance degradation typically observed in low OWR OBDFs under high-temperature, high-density conditions. The superior overall performance of the ESOP-optimized system, achieved using cost-effective ESO as a raw material, constitutes a highly competitive and cost-efficient solution for formulating ultra-low OWR drilling fluids in challenging deep-well applications. This performance, notably achieving a demulsification voltage exceeding 1200 V under the extreme dual conditions of an ultra-low 60:40 OWR and dynamic aging at 180°C, clearly benchmarks against and outperforms the typical performance ranges (e.g., demulsification voltages commonly reported between 800–1100 V) of most hyperbranched emulsifiers documented in prior studies, which were often validated under milder conditions such as higher OWRs (e.g., 80:20) or lower temperatures [27]. This underscores the distinctive advantage conferred by the ESOP molecular design and its synergistic formulation. A direct performance comparison with previously reported hyperbranched emulsifier systems is provided in Table 9, which clearly highlights the superior stability of our ESOP-based system under more challenging ultra-low OWR and high-temperature conditions.

Table 8: Comprehensive performance comparison of different OBDF systems after hot-rolling at 180°C for 16 h.

System	PV (mPa·s)	YP (Pa)	Demulsification Voltage (V)	HTHP FL (mL)	SF
Base Formulation	29	5.9	468	3.9	0.522
Commercial Emulsifier	32	8.6	812	2.4	0.511
ESOP-Optimized Formulation	36	9.8	1075	1.9	0.509

Table 9: A direct performance comparison of different OBDF systems after hot-rolling at 180°C for 16 h.

System Description	OWR	Aging Temp./°C	Demulsification Voltage (V)	HTHP FL (mL)	SF	Ref
Hyperbranched polyamide (Wei JY, 2024)	80:20	180	≥800	≤3	Not reported	[27]
ESOP-Optimized(without HNs)	60:40	180	1075	1.9	0.509	Table 8
ESOP-Optimized(with HNs)	60:40	180	1290	1.5	0.504	Table 10

Table 10: Performance enhancement of the OBDF system by HNs.

System	PV (mPa·s)	YP (Pa)	HTHP FL (mL)	Demulsification Voltage (V)	SF
ESOP-Optimized Formulation	34	11.8	1.9	1072	0.509
ESOP-Optimized (with HNs)	36	12.9	1.5	1290	0.504

3.3.2 Emulsification Stability

Emulsion stability is fundamental to maintaining the overall properties of OBDFs, thereby ensuring the safety of drilling operations. The minimum voltage required for demulsification of the emulsion is called the demulsification voltage, and the higher the value, the more stable the drilling fluid. The demulsification voltage of OBDF is typically required to exceed 800 V in field applications [39]. The emulsification stability, quantified by the demulsification voltage, of the three OBDF systems after exposure to different aging temperatures is presented in Fig. 4. As anticipated, the ES of all systems was progressively compromised by increasing thermal stress. The Base Formulation exhibited the most severe degradation, with its ES plummeting below the critical 800 V threshold after aging at 180°C, indicating imminent emulsion breakdown. The Commercial Emulsifier Formulation demonstrated better but still limited thermal resistance, maintaining ES above 800 V until 180°C, but showing a consistent declining trend.

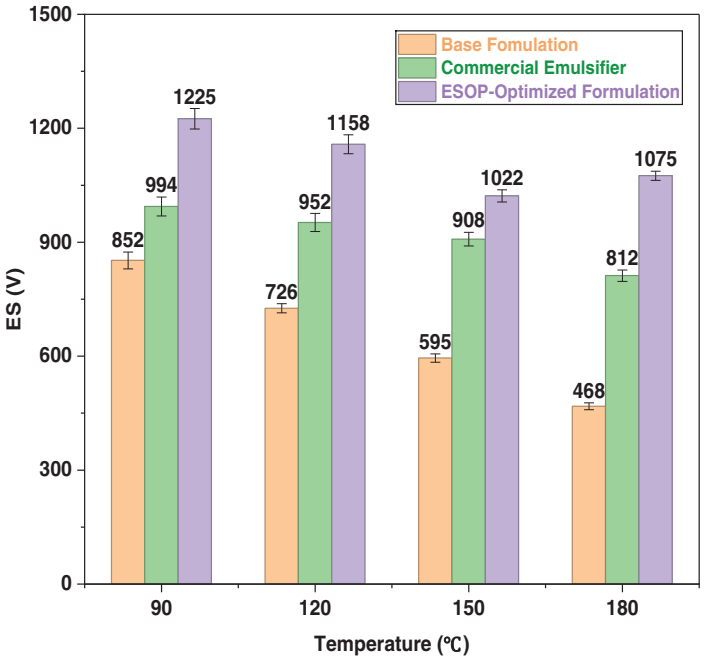

Figure 4: Variation of ES with thermal aging temperature for different OBDF systems.

In stark contrast, the ESOP-Optimized Formulation exhibited exceptional thermal resilience. Notably, it exhibited a significant rebound in ES at 180°C, suggesting a thermally-triggered self-reinforcement mechanism within the ESOP/CPS interfacial film, as will be discussed in Section 3.4.2. After 180°C aging,

the ESOP system's demulsification voltage was 1075 V, which is 96% and 34% higher than that of the base and commercial formulations, respectively, conclusively proving its superior ability to preserve emulsion stability under ultra-high temperature conditions.

3.3.3 Sag Stability under High-Density Conditions

Sag stability under thermal and inclined conditions was rigorously evaluated. As shown in Fig. 5a, the SF of all systems increased with aging temperature, yet the ESOP-Optimized Formulation consistently exhibited the lowest values, achieving an excellent SF of 0.509 after 180°C aging. This surpassed both the Base (0.522) and Commercial (0.511) formulations, with the former breaching the 0.52 warning threshold. The critical advantage under deviated wellbore conditions is revealed in Fig. 5b. After 180°C aging, the ESOP-optimized fluid maintained SF values below 0.52 at all inclination angles (0°, 45°, 90°), demonstrating isotropic stability. In contrast, both comparative formulations exceeded the safe limit at 45° and/or 90° inclinations, highlighting their vulnerability in horizontal sections. This performance aligns with observations in other studies where effective 3D network formation is crucial for mitigating angle-dependent sag.

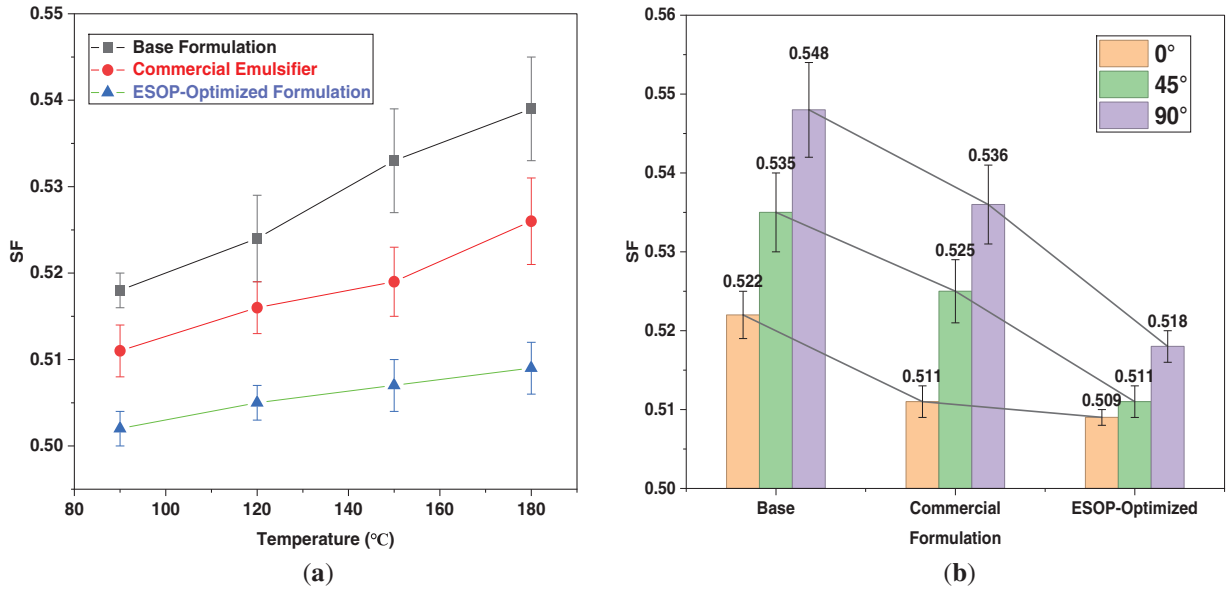

Figure 5: (**a**) Variation of SF with thermal aging temperature for different OBDF systems. (**b**) SF of different OBDF systems under various static inclination angles after hot-rolling at 180°C.

This superior, full-spectrum sag resistance is directly attributable to the unique microstructure of the ESOP-based system. The hyperbranched ESOP polymer, synergizing with HNs, forms a robust, three-dimensional network within the continuous oil phase. This network provides uniform gel strength that effectively suspends barite against both thermal degradation and the enhanced settling forces in inclined wellbores, a fundamental structural advantage over conventional linear emulsifiers.

3.3.4 HTHP FL

As illustrated in Fig. 6, the HTHP FL for all systems increased with aging temperature, indicating thermal degradation of the filter cake. The ESOP-Optimized Formulation consistently maintained the lowest filtration loss across the entire temperature range. After 180°C aging, it achieved an ultra-low filtration loss of only 1.9 mL (Table 8), which is approximately 67% and 48% lower than that of the base and commercial

formulations, respectively. This demonstrates the superior and stable filtration control provided by the synergistic ESOP/CPS/HNs system. This superior performance stems from a synergistic effect: the stable emulsion formed by the ESOP/CPS system minimizes aqueous phase invasion, while the HNs provide a "nano-filling" effect, plugging microscopic pores in the filter cake to form a denser, less permeable barrier. This combination ensures outstanding filtration control under high-temperature, high-pressure conditions.

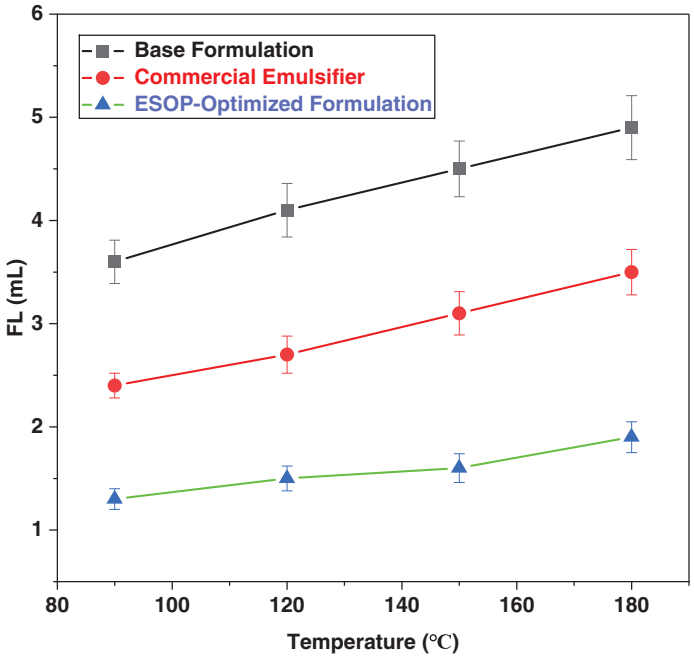

Figure 6: Variation of HTHP FL with thermal aging temperature for different OBDF systems.

3.3.5 Biological Toxicity Tests

According to the industry standard Q/SY 111–2007 (Luminescent bacteria test), the EC_{50} values of the drilling fluids were determined [40], and the results are listed in Table 11. The EC_{50} results of the three groups of samples are as follows: 25,200 mg/L (Base Formulation), 33,250 mg/L (Commercial Emulsifier), 38,900 mg/L (ESOP-Optimized Formulation). According to the biological toxicity grade classification standard, when the EC_{50} was larger than 25,000 mg/L, OBDF was nontoxic. If the EC_{50} exceeded 30,000 mg/L, the emission standard was achieved [41]. Therefore, both the Commercial Emulsifier and ESOP-Optimized formulations are classified as non-toxic. The ESOP-Optimized Formulation exhibited the highest EC_{50} value, indicating its superior environmental compatibility.

Table 11: Biotoxicity of different drilling fluid samples.

Sample	EC_{50}, mg/L	Biotoxicity
Base Formulation	25,200	Non-toxic
Commercial Emulsifier	33,250	Non-toxic
ESOP-Optimized Formulation	38,900	Non-toxic

3.3.6 Performance Enhancement with HNs

The incorporation of HNs into the optimized ESOP/CPS formulation led to comprehensive performance enhancements, as quantitatively demonstrated in Table 10. The demulsification voltage increased to 1290 V, HTHP fluid loss was reduced to 1.5 mL, and the SF decreased to a near-ideal 0.504, collectively confirming the critical role of HNs in fortifying the ultra-low OWR system under extreme conditions. Beyond these numerical gains, HNs impart essential robustness for field applications—under simulated downhole conditions of 180°C aging, 1.8 g/cm^3 density, and a challenging 60:40 OWR, they reinforce both the interface and the continuous phase through Pickering stabilization (forming a mechanical barrier against droplet coalescence) and a nano-filling effect (yielding a denser, less permeable filter cake). These multi-faceted mechanisms, which synergize with the molecular-scale actions of ESOP and CPS, are elaborated in the following section (Section 3.4). Together, they ensure long-term thermal and mechanical stability, making the HN-enhanced system a reliable candidate for demanding drilling operations.

3.4 Unraveling the Multi-Scale Synergistic Mechanism

The exceptional performance of the ESOP-optimized OBDF system, particularly its ability to maintain high stability at the ultra-low OWR of 60:40 under extreme thermal aging, stems from a multi-scale synergistic mechanism. This section delineates the underlying mechanisms across different scales, from molecular interactions to bulk phase structuring, which collectively confer the observed high-temperature stability and sag resistance under the specific condition of a minimized oil phase. A central finding is the thermally triggered self-reinforcement effect observed at the interface, which is pivotal for countering performance decay at 180°C. These mechanisms are conceptually summarized in Fig. 7. Direct visualization of these microstructures (e.g., via Cryo-SEM or CLSM) will be a key focus of future work to further substantiate these insights specific to ultra-low OWR systems.

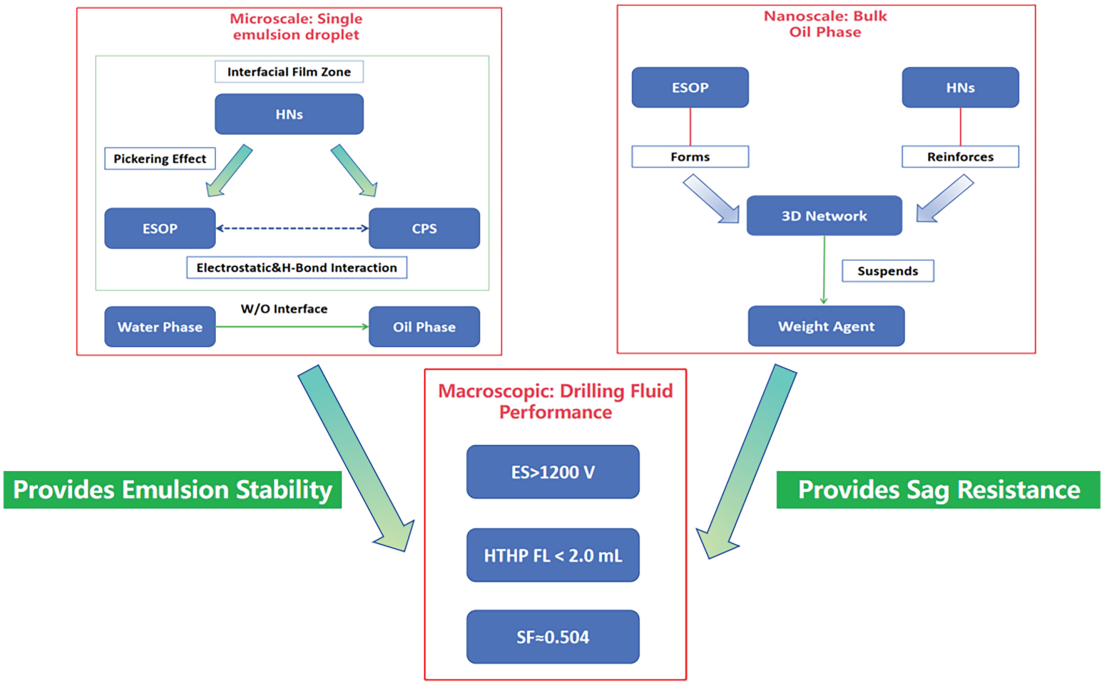

Figure 7: Multi-scale synergistic mechanism of the ultra-low OWR drilling fluid.

3.4.1 Molecular Architecture and Interfacial Synergy

The molecular foundation lies in the hyperbranched structure of ESOP. The synergy primarily originates from electrostatic attraction and hydrogen bonding between the amide groups of ESOP and the sulfonate groups of CPS. These molecular interactions facilitate the formation of a densely packed composite layer at the interface. The incorporation of HNs introduces Pickering stabilization. These nanoparticles become irreversibly adsorbed at the oil-water interface, forming a robust physical barrier that mechanically impedes droplet coalescence. This nanoscale "armor" synergizes with the molecular-scale ESOP/CPS film, creating a multi-level defense system, reflected in the remarkable surge in demulsification voltage upon HN's addition (Table 8).

3.4.2 Thermally Activated Interfacial Reinforcement

Zeta potential and particle-size analyses collectively unveiled a unique thermally triggered self-reinforcement mechanism in the ESOP-optimized system. Unlike the base and commercial formulations, whose Zeta potentials declined after thermal aging, the ESOP-optimized system exhibited a marked increase to –39.44 mV after 180°C aging (Fig. 8), indicating enhanced ionization or structural rearrangement under heat [42]. Concurrently, the average ESOP aggregate size decreased systematically from ~260 to ~145 nm (Fig. 9), a refinement synergistic with the Zeta potential trend and indicative of interfacial reorganization. This phenomenon, where elevated temperature refines emulsifier aggregates, aligns with observations of thermally-driven interfacial reorganization in other complex fluid systems [43]. Proposed mechanisms include: thermally promoted rearrangement of ESOP/CPS into a denser composite film [44]; conformational contraction of hyperbranched ESOP into smaller, more surface-active aggregates and strengthened ESOP–CPS interaction, facilitating compact composite micelles [45]. This self-reinforcing interfacial behavior underpins the anomalous rebound in demulsification voltage and record-high electrical stability after extreme thermal aging.

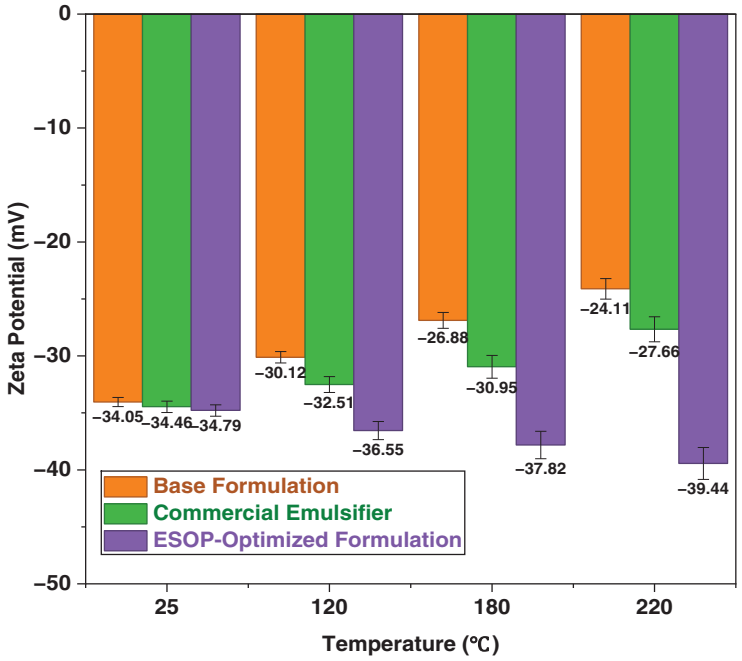

Figure 8: Zeta potential of different drilling fluid systems at varying temperatures.

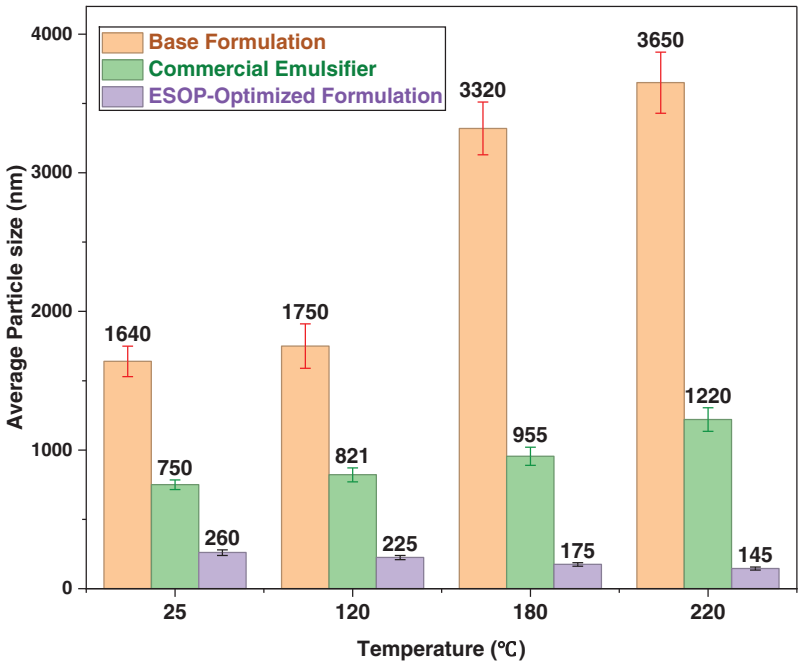

Figure 9: Particle size of different drilling fluid systems at varying temperatures.

3.4.3 Bulk Phase Network and Sag Stabilization

Beyond the interface, the ESOP/CPS/HNs system constructs a weak but effective three-dimensional network within the continuous oil phase. The hyperbranched ESOP molecules form the network backbone, while HN nanoparticles act as multifunctional cross-linking points. The efficacy of this network is quantitatively demonstrated by the marked increase in YP (e.g., from 11.8 to 12.9 Pa after 180°C aging, Table 10) and the SF of 0.509, which provides the necessary gel strength to suspend barite particles under static conditions.

3.4.4 Synergistic Filtration Control Mechanism

The ultra-low HTHP FL is a direct result of synergistic effects at the filter cake. The first line of defense is the exceptionally stable emulsion with small, uniformly sized droplets, which minimizes aqueous phase invasion. This effect is proposed to be augmented by the "nano-filling" effect of HNs, where the HNs likely plug microscopic pores within the filter cake under HTHP conditions, drastically reducing its permeability. This proposition is supported by the significant reduction in FL upon HN addition (Table 10) and is consistent with reports in the literature on nanoparticle-stabilized drilling fluids.

3.4.5 Interfacial Synergy and Its Microstructural Consequences

Direct evidence for the molecular synergy and stabilization mechanisms was obtained through interfacial and microstructural analyses. As shown in Fig. 10, the IFT measurements of the individual components vs. their combination revealed the core of the synergy: the ESOP/CPS blend reduced the IFT to 2.1 mN/m, markedly lower than ESOP (5.9 mN/m) or CPS (8.4 mN/m) alone, confirming cooperative adsorption and dense composite film formation. Consequently, emulsions stabilized by this synergistic system exhibited fine, uniform droplets. The addition of HNs sharply narrowed the droplet size distribution (PDI from 0.23 to 0.15) without changing the mean size, definitively characterizing their role as Pickering stabilizers that enhance homogeneity through steric hindrance.

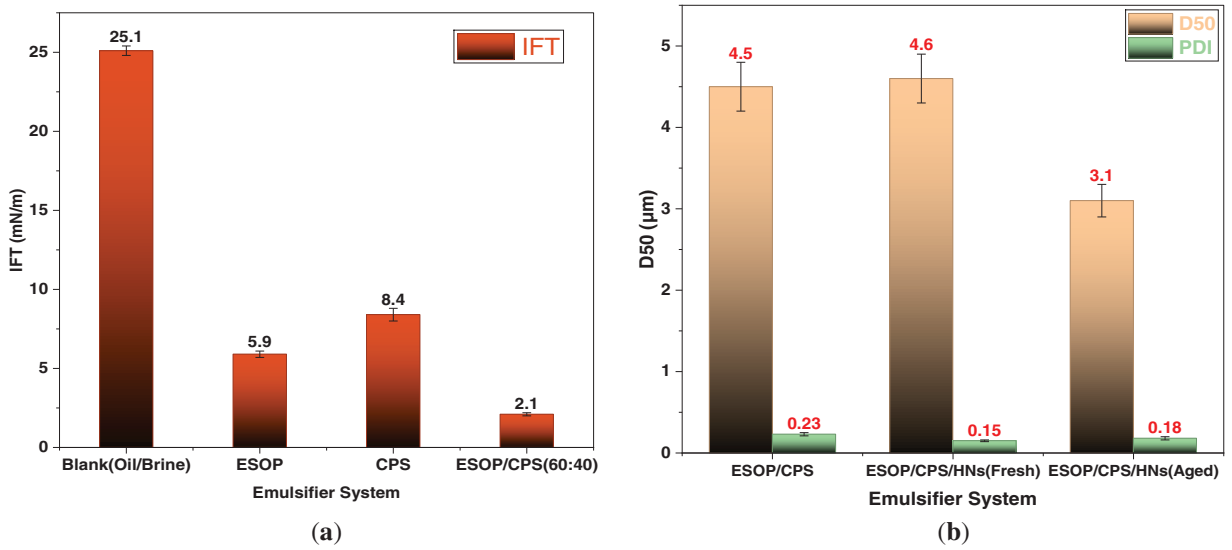

Figure 10: (**a**) IFT between white oil and 30% $CaCl_2$ solution for different emulsifier systems. (**b**) Droplet size distribution of fresh emulsions stabilized by the ESOP/CPS system with and without HNs.

The microstructural evolution under heat provides direct proof of interfacial self-reinforcement. As shown in Table 12, thermal aging at 180°C reduced the average droplet size in the ESOP/CPS/HNs system from 4.5 to 3.1 μm. This compaction visually corroborates the proposed densification mechanism, linking molecular-scale reorganization (Section 3.4.2) to the macroscopic rebound in emulsion stability (Fig. 4), thereby completing the mechanistic rationale for the exceptional high-temperature performance.

Table 12: Summary of interfacial and microstructural data.

Part 1: Interfacial tension of different emulsifier systems.	
Emulsifier System	**IFT (mN/m)**
Blank(Oil/Brine)	25.1 ± 0.3
ESOP only	5.9 ± 0.2
CPS only	8.4 ± 0.4
ESOP/CPS(60:40)	2.1 ± 0.1

Part 2: Emulsion droplet size characteristics for different emulsifier systems.		
Emulsifier System	D50 (μm)	PDI
ESOP/CPS	4.5 ± 0.3	0.23 ± 0.02
ESOP/CPS/HNs(Fresh)	4.6 ± 0.3	0.15 ± 0.01
ESOP/CPS/HNs(Aged)	3.1 ± 0.2	0.18 ± 0.02

4 Conclusions and Recommendations

This study demonstrates that a synergistic system integrating molecularly designed hyperbranched topology and tailored colloidal additives can effectively stabilize oil-based drilling fluids under the demanding condition of an ultra-low OWR of 60:40. The hyperbranched polyamide emulsifier (ESOP), synthesized

from epoxidized soybean oil, exhibits intrinsic thermal stability and facilitates multi-site interfacial anchoring. In combination with CPS and HNs, the formulated fluid achieves benchmark performance after 180°C aging, and a density of 1.8 g/cm^3 at an OWR of 60:40, achieves benchmark-setting macro-properties: a high demulsification voltage of 1290 V, an ultra-low HTHP fluid loss of 1.5 mL, and superior sag resistance (SF = 0.504). The success of this system is attributed to a multi-scale stabilization strategy uniquely effective at low oil content, which encompasses the formation of a dense composite interfacial film, pickering stabilization by HNs, a reinforcing three-dimensional network in the continuous phase, and a unique thermally triggered interfacial self-reinforcement mechanism. Beyond delivering a high-performance emulsifier for ultra-low OWR applications, this work establishes a general molecular topology engineering paradigm, highlighting that the rational design of hyperbranched architectures demonstrated here represents a versatile strategy for stabilizing a wide spectrum of complex industrial fluids under demanding thermal and mechanical stresses.

Limitations and Future Work:

This study provides strong indirect and correlative evidence for the proposed multi-scale stabilization mechanisms—such as the composite interfacial film, Pickering stabilization, 3D network, and thermally-triggered self-reinforcement—through macroscopic performance data, interfacial property measurements, and colloidal characterization. However, direct microstructural visualization of these mechanisms remains a limitation of the present work.

To furnish more conclusive evidence and deepen the mechanistic understanding, future work will focus on:

1. Advanced Downhole Simulation: Future work should employ advanced rheometers equipped with pressure cells to evaluate the fluid's performance under continuous shear and authentic pressure-temperature cycles that mimic ultra-deep well conditions more accurately.
2. Direct Microstructural Visualization: Use techniques such as cryo-SEM, confocal laser scanning microscopy (CLSM), or micro-CT to directly visualize the interfacial film, 3D network, and filter-cake microstructure, providing unequivocal visual evidence for the proposed mechanisms.
3. Comprehensive Ecotoxicity Assessment: Conduct multi-species toxicity tests (e.g., with algae or crustaceans) for a more comprehensive environmental risk assessment.
4. Pilot-scale Synthesis and Field Trials: The economic feasibility and consistency of ESOP synthesis should be validated at a pilot scale. Subsequent field trials are essential to demonstrate the practical efficacy, long-term stability, and economic benefits of this novel system in a real drilling environment.

Acknowledgement: None.

Funding Statement: This work was supported by the Key Research and Development Program Project of Hubei Province (2023BCB070).

Author Contributions: Conceptualization, Junping Wang, Mingbiao Xu; data curation, Junping Wang; writing—original draft preparation, Junping Wang; formal analysis, Wei Xiao; writing—review and editing, Junping Wang. All authors reviewed and approved the final version of the manuscript.

Availability of Data and Materials: The data that support the findings of this study are available from the corresponding author upon reasonable request.

Ethics Approval: Not applicable.

Conflicts of Interest: The authors declare no conflicts of interest.

References

1. Al-Ziyadi H, Verma A. Investigating the synergistic effects of coconut coir fiber and xanthan gum on the rheology and filtration loss of water-based drilling fluids. Petrol Sci Technol. 2024:1–17. doi:10.1080/10916466.2024.2445696.
2. Al-Ziyadi H, Pandian S, Verma A. Utilization of silica microfiber to enhance the rheological properties and fluid loss control of water-based drilling fluids. Energy Sources Part A Recovery Util Environ Eff. 2025;47(1):5027–40. doi:10.1080/15567036.2025.2464952.
3. Jin H, Liu L, Zhang M. Optimization of low-carbon drilling fluid systems and wellbore stability control for Shaximiao Formation in Sichuan Basin with a 'dual carbon' background. Processes. 2025;13(9):2859. doi:10.3390/pr13092859.
4. Medhi S, Chowdhury S, Dehury R, Khaklari GH, Puzari S, Bharadwaj J, et al. Comprehensive review on the recent advancements in nanoparticle-based drilling fluids: properties, performance, and perspectives. Energy Fuels. 2024;38(15):13455–513. doi:10.1021/acs.energyfuels.4c01161.
5. Al-Yasiri MS, Al-Sallami WT, Alyasiri M, Tareq W. How the drilling fluids can be made more efficient by using nanomaterials. Am J Nano Res Appl. 2015;3(3):41–5. doi:10.11648/j.nano.20150303.12.
6. Mikhienkova EI, Lysakov SV, Neverov AL, Zhigarev VA, Minakov AV, Rudyak VY. Experimental study on the influence of nanoparticles on oil-based drilling fluid properties. J Petrol Sci Eng. 2022;208:109452. doi:10.1016/j.petrol.2021.109452.
7. Li J, Yang P, Guan J, Sun Y, Kuang X, Chen S. A new type of whole oil-based drilling fluid. Petrol Explor Dev. 2014;41(4):538–44. doi:10.1016/s1876-3804(14)60064-1.
8. Saasen A, Berntsen M, Løklingholm G, Igeltjørn H, Åsnes K. The effect of drilling fluid base-oil properties on occupational hygiene and the marine environment. SPE Drill Complet. 2001;16(3):150–3. doi:10.2118/73193-pa.
9. Abdo J, Haneef MD. Clay nanoparticles modified drilling fluids for drilling of deep hydrocarbon wells. Appl Clay Sci. 2013;86(1):76–82. doi:10.1016/j.clay.2013.10.017.
10. Bizmark N, Ioannidis MA. Nanoparticle-stabilised emulsions: droplet armouring vs. droplet bridging. Soft Matter. 2018;14(31):6404–8. doi:10.1039/c8sm00938d.
11. Osinowo OO, Ayorinde JO, Nwankwo CP, Ekeng OM, Taiwo OB. Reservoir description and characterization of Eni field Offshore Niger Delta, southern Nigeria. J Petrol Explor Prod Technol. 2018;8(2):381–97. doi:10.1007/s13202-017-0402-7.
12. Siddig O, Mahmoud AA, Elkatatny S. A review of the various treatments of oil-based drilling fluids filter cakes. J Petrol Explor Prod Technol. 2022;12(2):365–81. doi:10.1007/s13202-021-01427-4.
13. Bui B, Saasen A, Maxey J, Ozbayoglu EM, Miska S, Yu M. Viscoelastic properties of oil-based drilling fluids. Annu Trans Nord Rheol Soc. 2012;20:33–47. doi:10.2118/166727-ms.
14. Lin S, Lu Y, Liu Z, Lu W, Hu P. Novel water-based mud for low-permeable reservoir in South China Sea. Energies. 2023;16(4):1738. doi:10.3390/en16041738.
15. Shen Z, Zhang H, Yu X, Wang M, Gao C, Li S, et al. Experimental optimization of high-temperature-resistant and low oil—Water ratio high-density oil-based drilling fluid. Processes. 2023;11(4):1129. doi:10.3390/pr11041129.
16. Dai B, Xu P, Xu M, Jiang Q, Liu Q, Wang S. Synthesis and plugging effect of inverse emulsion polymerization microspheres (OPME) for oil-based drilling fluids. Arab J Chem. 2023;16(4):104577. doi:10.1016/j.arabjc.2023.104577.
17. Zhang Z, Dai B, Xu P. A submicron-scale plugging agent for oil-based drilling fluid synthesized using the inverse emulsion polymerization method. Polymers. 2023;15(13):2815. doi:10.3390/polym15132815.
18. Yang G. A new oil-based drilling fluid system for enhancing the stability of deep well settlement under high temperature and high pressure conditions. Chem Technol Fuels Oils. 2025;61(1):147–57. doi:10.1007/s10553-025-01848-5.
19. Liu F, Li Y, Wang X, Xia Z. Preparation and properties of reversible emulsion drilling fluid stabilized by modified nanocrystalline cellulose. Molecules. 2024;29(6):1269. doi:10.3390/molecules29061269.
20. Liu F, Li Y, Li X, Wang X. The phase inversion mechanism of the pH-sensitive reversible invert emulsion. Molecules. 2023;28(21):7407. doi:10.3390/molecules28217407.

21. Pu L, Xu P, Xu M, Song J, He M, Wei M. Enhanced stability of low oil-to-water ratio water-in-oil emulsions (oil-based drilling fluids): synergistic effect of nano-SiO_2 and emulsifiers. J Petrol Sci Eng. 2022;219(3):111053. doi:10.1016/j.petrol.2022.111053.
22. Khan M. Chemical and physical architecture of macromolecular gels for fracturing fluid applications in the oil and gas industry; current status, challenges, and prospects. Gels. 2024;10(5):338. doi:10.3390/gels10050338.
23. Zhang Y, Yu W. Synthesis of hyperbranched polymers and prospects for application in oilfield chemistry. Front Energy Res. 2022;10:894096. doi:10.3389/fenrg.2022.894096.
24. Koo MS, Abouzeid R, Shayan M, Wu Q. Performance of oil-based drilling mud modified by lignocellulose nanofiber-cottonseed oil-sucrose ester compounds at elevated temperatures. Ind Eng Chem Res. 2025;64(40):19459–69. doi:10.1021/acs.iecr.5c01970.
25. Wang H, Zou C. β-Cyclodextrin modified TiO_2 nanofluids to improve the stability and thermal conductivity of oil-based drilling fluids. Colloids Surf A Physicochem Eng Aspects. 2023;661:130957. doi:10.1016/j.colsurfa.2023.130957.
26. Wang T, Sun M, Pan Y, Fu L, Yang S. Development a new type of oil based drilling fluid with good temperature resistant. Energy Sources Part A Recovery Util Environ Eff. 2025;47(1):10764–78. doi:10.1080/15567036.2021.1970291.
27. Wei JY. Preparation and evaluation of hyperbranched emulsifiers for oil-based drilling fluids. Shandong Chem Ind. 2024;53(18):4–8. (In Chinese). doi:10.19319/j.cnki.issn.1008-021x.2024.18.001.
28. Rafati R, Smith SR, Sharifi Haddad A, Novara R, Hamidi H. Effect of nanoparticles on the modifications of drilling fluids properties: a review of recent advances. J Petrol Sci Eng. 2018;161(7):61–76. doi:10.1016/j.petrol.2017.11.067.
29. Magalhães SC, Calçada LA, Scheid CM, Almeida H, Waldmann ATA. Improving drilling performance with continuous online measurements of electrical stability and conductivity in oil based drilling fluids. J Petrol Sci Eng. 2016;146:369–79. doi:10.1016/j.petrol.2016.05.045.
30. Yang J, Wang R, Dong B, Ai Z, Peng L, Xie G. Investigating on the performance and mechanism of poly(styrene-methyl methacrylate-ethyl methacrylate-butyl acrylate) as nano sealing agent in oil-based drilling fluids. ACS Omega. 2024;9(40):41250–7. doi:10.1021/acsomega.4c03083.
31. Maxey J. Rheological analysis of static and dynamic sag in drilling fluids. Annu Trans Nord Rheol Soc. 2007;15:181. doi:10.2118/199567-pa.
32. Huang X, Sun J, Lyu K, Dong X, Liu F, Gao C. A high-temperature resistant and high-density polymeric saturated brine-based drilling fluid. Petrol Explor Dev. 2023;50(5):1215–24. doi:10.1016/s1876-3804(23)60460-4.
33. Li XL, Jiang GC, Xu Y, Deng ZQ, Wang K. A new environmentally friendly water-based drilling fluids with laponite nanoparticles and polysaccharide/polypeptide derivatives. Petrol Sci. 2022;19(6):2959–68. doi:10.1016/j.petsci.2022.07.003.
34. Wang L. Preparation and application of viscosifier for environmentally friendly oil-based drilling fluid. Chem Technol Fuels Oils. 2015;51(5):539–44. doi:10.1007/s10553-015-0637-2.
35. Sanders PF, Tibbetts PJC. Effects of discarded drill muds on microbial populations. Philos Trans R Soc Lond B Biol Sci. 1987;316(1181):567–85. doi:10.1098/rstb.1987.0039.
36. Smith B. Infrared spectral interpretation: A systematic approach. Boca Raton, FL, USA: CRC Press; 1998.
37. Smith BC. Infrared spectral interpretation, in the beginning I: the meaning of peak positions, heights, and widths. Spectroscopy. 2024:18–24. doi:10.56530/spectroscopy.fi6379n1.
38. Alabarse FG, Conceição RV, Balzaretti NM, Schenato F, Xavier AM. *In-situ* FTIR analyses of bentonite under high-pressure. Appl Clay Sci. 2011;51(1–2):202–8. doi:10.1016/j.clay.2010.11.017.
39. Liu L, Pu X, Zhou Y, Zhou J, Luo D, Ren Z. Smart Pickering water-in-oil emulsion by manipulating interactions between nanoparticles and surfactant as potential oil-based drilling fluid. Colloids Surf A Physicochem Eng Aspects. 2020;586:124246. doi:10.1016/j.colsurfa.2019.124246.
40. Ma XY, Wang XC, Ngo HH, Guo W, Wu MN, Wang N. Bioassay based luminescent bacteria: interferences, improvements, and applications. Sci Total Environ. 2014;468-469:1–11. doi:10.1016/j.scitotenv.2013.08.028.
41. Yang X, Shang Z, Liu H, Cai J, Jiang G. Environmental-friendly salt water mud with nano-SiO_2 in horizontal drilling for shale gas. J Petrol Sci Eng. 2017;156:408–18. doi:10.1016/j.petrol.2017.06.022.

42. Zhang H, Gao J, Wang H, Chen H, Dai H, Ma L, et al. Effect of tannic acid on the heat-induced flocculation of gelatin/cellulose nanocrystal-based emulsions: mechanisms behind the formation of high internal phase emulsion gels. Food Hydrocoll. 2026;170:111765. doi:10.1016/j.foodhyd.2025.111765.
43. Kim DH. Regioisomeric effect on the stereoscopic conformational transition of polymer monolayers at the aqueous interface. J Phys Chem Lett. 2025;16(9):2160–5. doi:10.1021/acs.jpclett.5c00069.
44. Maldonado-Valderrama J, del Castillo-Santaella T, Adroher-Benítez I, Moncho-Jordá A, Martín-Molina A. Thermoresponsive microgels at the air–water interface: the impact of the swelling state on interfacial conformation. Soft Matter. 2017;13(1):230–8. doi:10.1039/c6sm01375a.
45. Lezov A, Gubarev A, Kaiser T, Tobaschus W, Tsvetkov N, Nischang I, et al. "Hard" sphere behavior of "soft", globular-like, hyperbranched polyglycerols-extensive molecular hydrodynamic and light scattering studies. Macromolecules. 2020;53(21):9220–33. doi:10.1021/acs.macromol.0c01340.